Porous Ni0.14Mn0.86O1.43 hollow microspheres as high-performing anodes for lithium-ion batteries

Article *in* Journal of Power Sources · September 2015

DOI: 10.1016/j.jpowsour.2015.05.021

Zhong Ma
Shanghai Jiao Tong University

Yuan Xianxia
Shanghai Jiao Tong University

Zi-Feng Ma
Shanghai Jiao Tong University

Lei Zhang
National Research Council Canada

Journal of Power Sources 291 (2015) 156–162

Contents lists available at ScienceDirect

Journal of Power Sources

journal homepage: www.elsevier.com/locate/jpowsour

Porous $Ni_{0.14}Mn_{0.86}O_{1.43}$ hollow microspheres as high-performing anodes for lithium-ion batteries

Zhong Ma [a], Xianxia Yuan [a,*], Lin Li [a], Zi-Feng Ma [a], Lei Zhang [b], Liqiang Mai [c], Jiujun Zhang [b]

[a] Shanghai Electrochemical Energy Devices Research Center, Department of Chemical Engineering, Shanghai Jiao Tong University, Shanghai 200240, China
[b] Department of Chemical and Biochemical Engineering, University of British Columbia, Vancouver, BC V6T 1W5, Canada
[c] State Key Laboratory of Advanced Technology for Materials Synthesis and Processing, WUT-Harvard Joint Nano Key Laboratory, Wuhan University of Technology, Wuhan 430070, China

HIGHLIGHTS

- A novel strategy for uniformly dispersed bi-component nanocomposite.
- Porous and hollow-structured $Ni_{0.14}Mn_{0.86}O_{1.43}$ microspheres as anode for LIBs.
- $Ni_{0.14}Mn_{0.86}O_{1.43}$ exhibit excellent high rate capability and exciting lifespan.

GRAPHICAL ABSTRACT

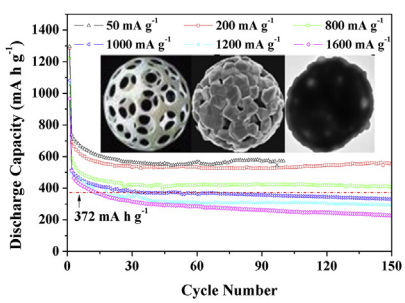

ARTICLE INFO

Article history:
Received 3 February 2015
Received in revised form
12 April 2015
Accepted 9 May 2015
Available online xxx

Keywords:
Lithium ion batteries
Anode
$Ni_{0.14}Mn_{0.86}O_{1.43}$
Porous & hollow microspheres

ABSTRACT

A uniformly dispersed bi-component nanocompotise of transition metal oxide (Mn_2O_3)/mixed transition metal oxide ($NiMn_2O_4$) with a porous and hollow microspheric sructure has been successfully prepared with a facile method based on the complexation between Ni^{2+} and NH_3. The obtained nanocomposite of 0.29 Mn_2O_3/0.14 $NiMn_2O_4$, expressed as $Ni_{0.14}Mn_{0.86}O_{1.43}$, with nanometer-sized building blocks exhibits a high reversible capacity of 615 mA h g^{-1}, which is about 90% of theoretical value at the current density of 800 mA h g^{-1}, and long lifespan with retained capacities of 553 and 408 mA h g^{-1} after 150 cycles at 200 and 800 mA g^{-1}, respectively, as an anode material for lithium-ion batteries.

1. Introduction

As recognized, Lithium ion batteries (LIBs) have a great potential in applications of electric vehicles and large-scale electric grids [1–4]. However, both the insufficient energy density and cycle-life of LIBs have limited their commercial usage in these applications. To overcome these two challenges, many kinds of electrode materials have been explored in most recent years [5–13]. Although graphite is the mostly used commercial anode material for LIBs, its low capacity, poor rate capability and safety problem seem to be the major drawbacks [2,14–16]. Among various non-graphite materials explored for LIBs anodes, transition-metal oxides (TMOs) are considered one type of the most promising materials due to their

* Corresponding author.
E-mail address: yuanxx@sjtu.edu.cn (X. Yuan).

http://dx.doi.org/10.1016/j.jpowsour.2015.05.021
0378-7753/

higher lithium storage capacities and better safety [6,9,17–19]. As identified, their lithium storage mechanism is different from the classical mechanisms based on reversible insertion/extraction of lithium into host structures or on lithium alloying reactions. This kind of TMO anode materials typically involves the formation/decomposition of Li_2O accompanying the reduction/oxidation of TMOs during the battery reaction [5,20,21]. Poizot et al. [22] studied the TMOs such as CoO, NiO, CuO and FeO as anodes of LIBs and found that CoO could obtain a reversible capacity of 700 mA h g^{-1} at a rate of 0.2C and keep 100% capacity retention for up to 100 cycles. Furthermore, the mixed transition-metal oxides (MTMOs) combining two simple TMOs or a TMO and a post-TMO (the oxide of post-transition metals located between the transition metals and the metalloids in the periodic table [23–25]) into spinel-like structures (AB_2O_4; A, B=Mn, Fe, Co, Ni, Zn, Cu, and so on, A ≠ B) with stoichiometric or even non-stoichiometric compositions could exhibit exceptionally high specific capacities due to both their complex chemical compositions and the synergetic effects [12,26–29]. Alcántara et al. [30] reported a Li cyclability of $NiCo_2O_4$ spinel for the first time in 2002. Thence, a large number of MTMOs with spinel structures have been demonstrated as anode materials for LiBs [27,31]. Moreover, TMOs or MTMOs with unique hierarchical micro-/nanostructures as secondary superstructures, where the particles are typically of micro-/submicrometer dimensions and internally consisted of nano-building blocks and/or nano-domains, could offer exceptional advantages of both nanometer-sized building blocks/nano-domains and micro-/submicrometer-sized assemblies [32,33]. For example, Zhou et al. [34] prepared the double-shelled $CoMn_2O_4$ hollow microcubes by co-precipitation/annealing method, and the as-prepared material delivered capacities of 1282 and 827 mA h g^{-1} at the first and second cycles, respectively, at a current density of 200 mA g^{-1} and sustained 624 mA h g^{-1} after 50 cycles. Liu et al. [35] prepared hierarchical three-dimensional $ZnCo_2O_4$ nanowire arrays based on hydrothermal method, which exhibited a reversible capacity of 1200 mA h g^{-1} after 160 cycles at 200 mA g^{-1}.

Most recently, assembling both TMOs and MTMOs into homogeneously dispersed bi-component material of TMO/MTMO with hierarchical structure has also been demonstrated to be an efficient strategy to improve the lithium storage performance. The well-dispersed bi-component-active $CoO/CoFe_2O_4$ nanocomposites developed by Li et al. [36] demonstrated a much higher capacity and also greatly improved cycle-ability than CoO, $CoFe_2O_4$ and the mechanically mixed $CoO/CoFe_2O_4$ as LIBs anode materials. The hierarchical $Fe_2O_3/NiFe_2O_4$ nanotubes derived from metal organic frameworks delivered apparently larger reversible charge–discharge capacity, much better cycling stability and superior rate capability than $NiFe_2O_4$ nanotubes, they retained a capacity of 936.9 mA h g^{-1} after 100 cycles at a current density of 100 mA g^{-1}, compared to that of 598.1 mA h g^{-1} for the latter [37]. However, there is no report, to the best of our knowledge, on the performance of a composite combining $NiMn_2O_4$ and another TMO, with specific morphology, as anode material for LIBs to date [38,39].

Herein, a novel porous and hollow-structured TMO/MTMO nanocomposite of $Ni_{0.14}Mn_{0.86}O_{1.43}$ (0.29 Mn_2O_3/0.14 $NiMn_2O_4$) microspheres was synthesized with a facile co-precipitation and annealing method based on the complexation between Ni^{2+} and NH_3. It demonstrated excellent high rate capability and exciting lifespan as anode material of LIBs.

2. Experimental

2.1. Chemicals

Analytical reagents of $Ni(NO_3)_2 \cdot 6H_2O$, $MnSO_4 \cdot H_2O$, NH_4HCO_3, $NaHCO_3$ and ethanol were purchased from Sinopharm Chemical Reagent Co., Ltd., Super-P-Li was from SCM Industrial Chemical Co., Ltd., 1 M $LiPF_6$ in a 1:1 v/v mixture of ethylene carbonate and dimethyl carbonate was from Shenzhen CAPCHEM Technology Co. Ltd., and Li foil was from China Energy Lithium Co., Ltd.. All the chemicals were used as received without further purification.

2.2. Materials synthesis

The porous and hollow-structured $Ni_{0.14}Mn_{0.86}O_{1.43}$ microspheres were prepared as follows: 1.67 mmol of $Ni(NO_3)_2 \cdot 6H_2O$, 3.33 mmol of $MnSO_4 \cdot H_2O$ and 35 ml of ethanol were dissolved in 350 ml of distilled water with vigorous stirring, 50 mmol of NH_4HCO_3 dissolved in 350 ml of distilled water was then added. The mixed solution was heated to 45 °C and maintained for 9 h with vigorous stirring. The precipitate was then collected by filtration, washed thoroughly with distilled water and dried at 60 °C overnight in vacuum. The obtained carbonate precursor was heat-treated in air at 600 °C for 3 h and at 900 °C for 2 h in sequence at a temperate ramp of 2 °C min^{-1}.

NiO and Mn_2O_3 were also prepared for comparison by the same method with 5 mmol of $Ni(NO_3)_2 \cdot 6H_2O$ and $MnSO_4 \cdot H_2O$, respectively. $NiMn_2O_4$ was synthesized via the same method using $NaHCO_3$ instead of NH_4HCO_3 as the precipitator.

2.3. Materials characterization

The phase components and structure of the as-prepared materials were characterized using Bruker D8 Advanced X-Ray Diffractometer. Morphology of the materials was obtained on FEI Nova NanoSEM 450 Field-Emission Scanning Electron Microscope (FESEM) and JEOL 2100F Field-Emission Transmission Electron Microscopy (FETEM). The composition of the samples was analyzed by EDX attached to the FESEM instrument. Thermogravimetric Analysis (TGA) was carried out under air flow with a temperature ramp of 10 °C min^{-1} on Netzsch STA 449 F3 Jupiter instrument. The Mn and Ni content in the carbonate precursor and as-prepared oxide were quantified using a Thermal iCAP 6300 Inductive Coupled Plasma (ICP) spectrometer.

2.4. Electrochemical measurements

The electrochemical measurements were carried out on CR2016 type coin cells. The working electrodes were made of 70 wt% active oxide materials, 20 wt% Super-P-Li as the conductive agent and 10 wt% polyvinylidene fluoride (PVDF) as the binder. Metallic lithium foil was used as the counter electrode and 1 M $LiPF_6$ in a 1:1 v/v mixture of ethylene carbonate and dimethyl carbonate was the electrolyte. Cells were assembled in an Ar-filled glovebox with moisture and oxygen concentrations below 0.1 ppm. Cyclic voltammetry measurements were performed on a CHI 750A electrochemical potentiostat/galvanostat at a potential scanning rate of 0.1 mV s^{-1}. The galvanostatic charge–discharge tests were performed on a LAND CT2001A battery tester in the voltage range of 0.01–3 V *vs.* Li/Li^+.

3. Results and discussion

Fig. 1 is a schematic diagram of the fabrication mechanism of the porous and hollow-structured $Ni_{0.14}Mn_{0.86}O_{1.43}$ microspheres. $Ni_{0.14}Mn_{0.86}CO_3$ microspheres were firstly formed by co-precipitation of NH_4HCO_3, $Ni(NO_3)_2 \cdot 6H_2O$ and $MnSO_4 \cdot H_2O$ as shown in Fig. 1a. During this process, the $Ni_{0.14}Mn_{0.86}CO_3$ uniform microspheres (Fig. 2a, Figs. S1 and S2) were formed with $MnCO_3$ microspheres (Fig. 2b, Figs. S3 and S4) as the body and $NiCO_3$

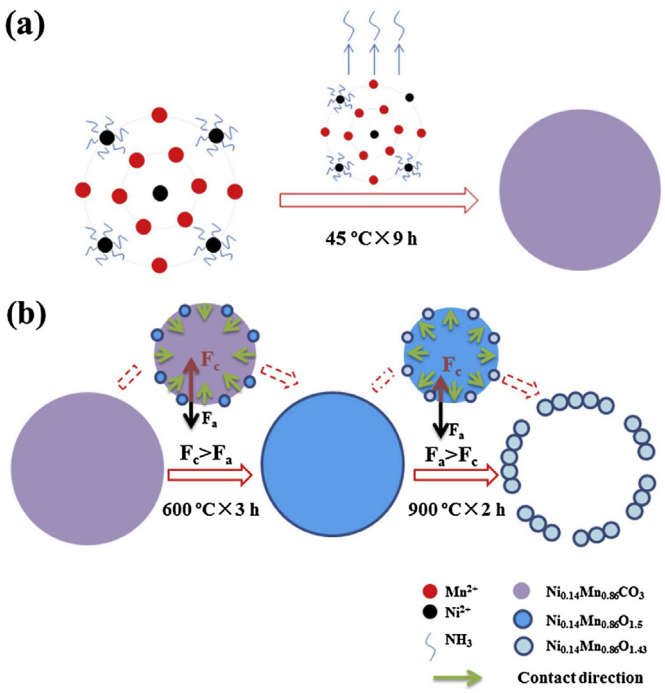

Fig. 1. Schematic illustration of the fabrication mechanism of $Ni_{0.14}Mn_{0.86}CO_3$ microspheres (a) and porous $Ni_{0.14}Mn_{0.86}O_{1.43}$ hollow microspheres (b).

powders (Fig. 2c and Fig. S5) as the ornament, and the deposition rate of $NiCO_3$ played an important role on the formation of morphology/structure of the microspheres owing to the complexation between Ni^{2+} and NH_3. Specifically, the nickelhexammine complex firstly formed in the precipitating solution by $Ni^{2+} + 6NH_3 \rightarrow [Ni(NH_3)_6]^{2+}_{(aq)}$, where NH_3 was from the hydrolysis of ammonium ion from NH_4HCO_3 in the solution by $NH_4^+ + H_2O \leftrightarrow NH_3 + H^+ \cdot H_2O$ [40,41]. Then, with the removal of ammonia from the solution by $[Ni(NH_3)_6]^{2+}_{aq} \rightarrow Ni^{2+} + 6NH_3\uparrow$ because of the heating, the concentration of ammonia in the solution decreased and the free nickel ions increased. When the concentration of nickel ions reached a certain level, $NiCO_3$ precipitated homogeneously in the solution. The deposition of $NiCO_3$ was thus so slow that it did not wreck but modified and regulated the morphology of $MnCO_3$ microspheres into Phoenix tree balls with shaped edges (Fig. 2a, Figs. S1 and S2) rather than that with square corners of pure $MnCO_3$ (Fig. 2b, Figs. S3 and S4). This can also explain the fact that the atom ratio of Ni:Mn in the final product, 0.14:0.86 (will be discussed below), is different from that of 1:2 in the precipitating solution. When the precipitator was $NaHCO_3$ instead of NH_4HCO_3, however, the complexation disappeared and the deposition of $NiCO_3$ was too fast to form microspheres (Fig. 2d and Fig. S6).

The $Ni_{0.14}Mn_{0.86}CO_3$ uniform microspheres were subsequently annealed at 600 °C for 3 h and 900 °C for 2 h, respectively, with a temperature ramping rate of 2 °C min^{-1} to convert $Ni_{0.14}Mn_{0.86}CO_3$ into $Ni_{0.14}Mn_{0.86}O_{1.43}$ compound with a hollow and porous structure (Fig. 1b) based on the heterogeneous contractions during the heat-treatment process [34,42]. During the annealing at 600 °C for 3 h, the surface $Ni_{0.14}Mn_{0.86}CO_3$ microspheres were firstly transformed into $Ni_{0.14}Mn_{0.86}O_{1.5}$ (0.36 Mn_2O_3/0.14 $NiMnO_3$, as shown in Fig. 3) as a shell, induced by the large temperature gradient (ΔT) along the radial direction [43]. Then, two forces in opposite directions (the so-called heterogeneous contraction) acted on the interface between the $Ni_{0.14}Mn_{0.86}O_{1.5}$ shell and the $Ni_{0.14}Mn_{0.86}CO_3$ core. The contraction force (F_c) induced by the weight loss during Step 2 in Fig. S7 promoted the inward shrinkage of the $Ni_{0.14}Mn_{0.86}CO_3$ core, while the adhesion force (F_a) from the relatively rigid shell restricted this inward contraction. Owing to both the large weight loss (Step 2 in Fig. S7) and the minimization of surface energy, F_c surpassed F_a and $Ni_{0.14}Mn_{0.86}CO_3$ microspheres

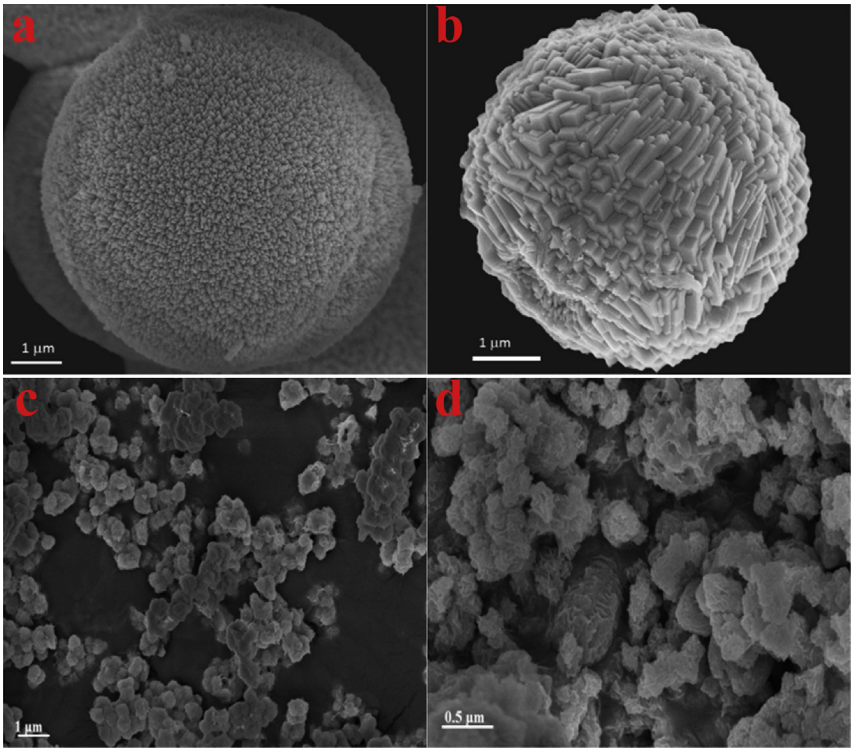

Fig. 2. FESEM images of the $Ni_{0.14}Mn_{0.86}CO_3$ microsphere (a), $MnCO_3$ microsphere (b), $NiCO_3$ powders (c) and $Ni_{0.33}Mn_{0.67}CO_3$ powders (d).

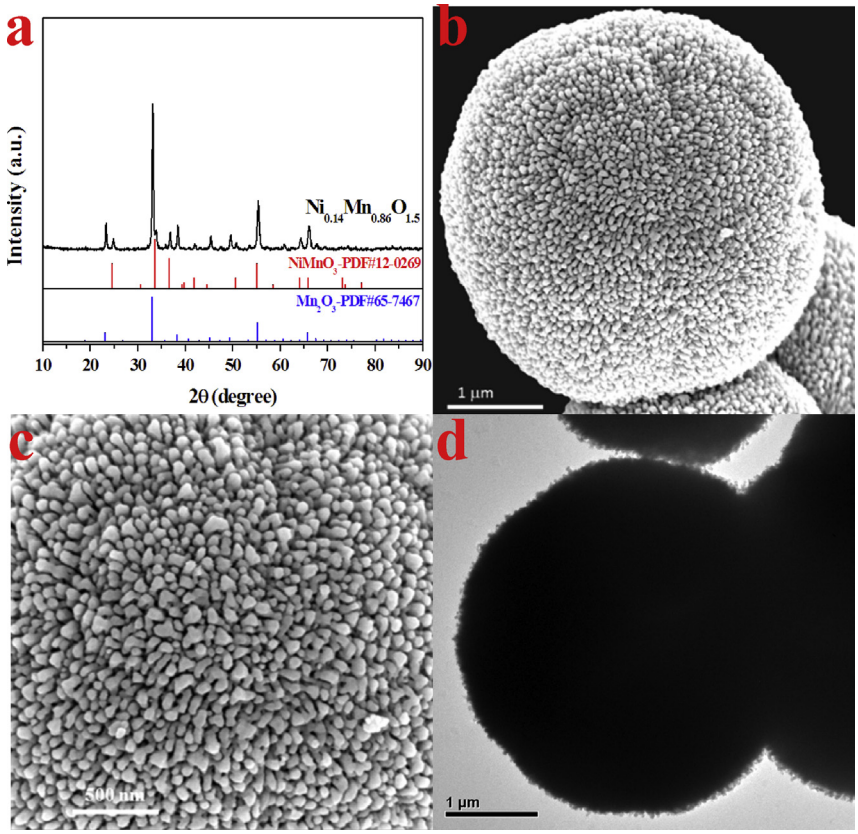

Fig. 3. XRD pattern (a), FESEM (b, c) and FETEM (d) images of $Ni_{0.14}Mn_{0.86}O_{1.5}$ solid microsphere.

shrank into solid waxberry-like $Ni_{0.14}Mn_{0.86}O_{1.5}$ microspheres (Fig. 3). During the subsequent pyrolysis at 900 °C for 2 h, the solid waxberry-like $Ni_{0.14}Mn_{0.86}O_{1.5}$ microspheres were also heated with heterogeneous contraction. At the initial stage of calcination, $Ni_{0.14}Mn_{0.86}O_{1.43}$ shell firstly formed on the surface of the $Ni_{0.14}Mn_{0.86}O_{1.5}$ core. And then, the adhesion force (F_a) between the $Ni_{0.14}Mn_{0.86}O_{1.43}$ shell and the $Ni_{0.14}Mn_{0.86}O_{1.5}$ core surpassed the contraction force (F_c) caused by the small weight loss during step 3 in Fig. S7, leading to shrinkage of the inner core outward, leaving a hollow cavity in the center. Meanwhile, Ostwald ripening also happened during this elevated temperature calcination process, making contribution to the resulted porous structure.

Fig. 4a is the X-ray diffraction (XRD) pattern of the as-prepared material. All the characteristic peaks could be assigned to $NiMn_2O_4$ (JCPDF Card No. 01-1110, space group: cubic (face-center), $a = b = c = 8.3824$ Å, $\alpha = \beta = \gamma = 90°$) and Mn_2O_3 (JCPDF Card No. 65-7467, space group: Ia-3, $a = b = c = 9.408$ Å, $\alpha = \beta = \gamma = 90°$). The weight percentage of Ni and Mn in this material measured with ICP was 10.3% and 61.3%, respectively. Therefore, the atom ratio of Ni:Mn was calculated to be 0.14:0.86, and the molecular formula of the as-prepared material was expressed as $Ni_{0.14}Mn_{0.86}O_{1.43}$ (0.29 Mn_2O_3/0.14 $NiMn_2O_4$).

Field-Emission Scanning Electron Microscopy (FESEM) and Field-Emission Transmission Electron Microscopy (FETEM) were employed to characterize the morphology and detailed structure of the prepared $Ni_{0.14}Mn_{0.86}O_{1.43}$ microspheres. An overall view is shown as Fig. 4b, the as-prepared material has a morphology of very uniform microspheres in a diameter of about 5 μm and each microsphere (Fig. 4c) is consisted of numerous layered nano-building blocks (Fig. 4d) accumulated with porous structure. The molar ratio of Mn:Ni, acquired by energy-dispersive X-ray spectroscopy (EDX) attached to FESEM, is about 6 (Fig. S8), agreeing well with the ICP results. The SEM-Mapping images of various elements in a single $Ni_{0.14}Mn_{0.86}O_{1.43}$ microsphere (Fig. S9) indicate that Ni, Mn and O are uniformly dispersed in the whole microsphere and the amounts of Mn and O are drastically higher than that of Ni. TEM image of the as-synthesized $Ni_{0.14}Mn_{0.86}O_{1.43}$ microspheres is shown as Fig. 4e. Because of the relatively large size of the microsphere (~5 μm) and nanoblocks (~500 nm), the hollow interiors are not distinct. However, there are several of the relatively light contrast areas at the center of the microsphere, illustrating the existence of the hollow interiors. Fig. 4f is the representative high-resolution TEM (HRTEM) image of the as-prepared $Ni_{0.14}Mn_{1.86}O_{1.43}$, both the (111) lattice space (0.485 nm) and (220) lattice space (0.297 nm) corresponding to $NiMn_2O_4$ and the (222) lattice space (0.271 nm) attributed to Mn_2O_3 can be clearly observed, implying again that the as-prepared porous and hollow-structured $Ni_{0.14}Mn_{1.86}O_{1.43}$ is a uniformly dispersed bi-component nanocomposite of 0.29 Mn_2O_3/0.14 $NiMn_2O_4$.

Cyclic voltammetery (CV) was employed to evaluate the electrochemical properties of the porous $Ni_{0.14}Mn_{0.86}O_{1.43}$ hollow microspheres, and the obtained curves are shown as Fig. 5a. Referring to the CV curves (Fig. 5b–d) of NiO, Mn_2O_3 and $NiMn_2O_4$ (Figs. S10–S12) prepared with the same procedure, the peak centered at ~1.3 V in the cathodic process of the first cycle should correspond to the reduction of Mn^{3+} to Mn^{2+}, while the broad peak at 0.55 V should correspond to the reduction of Ni^{2+} to metallic Ni and the formation of solid-electrolyte interface (SEI), and the sharp peak at ~0.15 V should correspond to the reduction of Mn^{2+} to metallic Mn. In the followed anodic sweep, the peak at ~1.28 V is derived from the oxidation of Mn to Mn^{2+} and the other one at ~2.10 V is due to the oxidation of Ni to Ni^{2+}. In the second and third

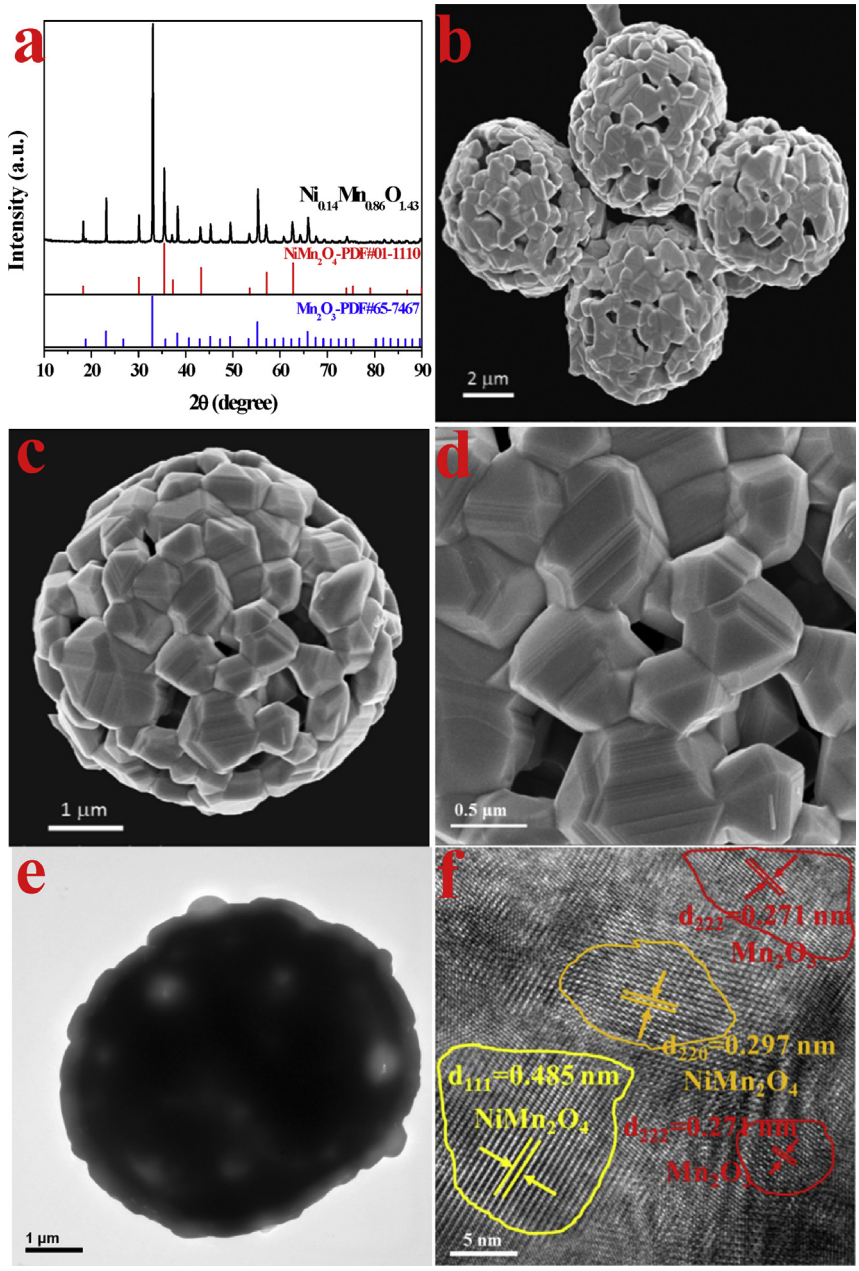

Fig. 4. XRD pattern (a), FESEM (b–d), FETEM (e) and HRTEM (f) images of porous $Ni_{0.14}Mn_{0.86}O_{1.43}$ hollow microspheres.

cycles, there appear two pairs of redox peaks. The one at 0.25/1.23 V corresponds to the reduction/oxidation of MnO while the other one at 0.94/2.16 V can be assigned to the reduction/oxidation of NiO.

The porous and hollow-structured $Ni_{0.14}Mn_{0.86}O_{1.43}$ microspheres were then evaluated as anode material of LIBs. Fig. 6a shows the representative charge–discharge profiles at a current density of 800 mA g^{-1}. The first cycle discharge capacity achieves at 1222 mA h g^{-1}, which is apparently higher than the theoretical value of 979 mA h g^{-1} (See the lithium storage mechanism in Supporting Information) probably owing to the irreversible formation of SEI film on the anode surface. Excitingly, the reversible charge capacity at such a high current density is 615 mA h g^{-1}, which is about 90% of the theoretical value (684 mA h g^{-1}, See the lithium storage mechanism in Supporting Information), although an irreversible capacity loss caused by the formation of SEI film on the anode surface has also been observed. Fig. 6b is the rate capability of the $Ni_{0.14}Mn_{0.86}O_{1.43}$ anode. At the current density of 50 mA g^{-1}, the reversible capacity is 771 mAh g^{-1}, which is much higher than the theoretical capacity and could be attributed to its complex chemical composition as well as the synergetic effects [37,44]. Furthermore, an excellent high rate capability could be achieved on $Ni_{0.14}Mn_{0.86}O_{1.43}$ with the discharge capacity retentions of 99%, 94%, 84%, 82%, 74% at 200, 800, 1000, 1200 and 1600 mA g^{-1}, respectively, when compared to that at 50 mA g^{-1} (Fig. 6b and Fig. S13).

The discharge/charge capacities as well as coulombic efficiency at various current densities versus cycle number in the voltage range of 0.01–3.0 V *vs.* Li/Li^+ are shown as Fig. 6c and Figs. S14–S19. As shown, the discharge capacity and the cycle-ability at a current density of 200 mA g^{-1} are very close to that at 50 mA g^{-1}, implying the excellent high-rate performance of the porous and hollow-structured $Ni_{0.14}Mn_{0.86}O_{1.43}$ microspheres. At 200 mA g^{-1}, the

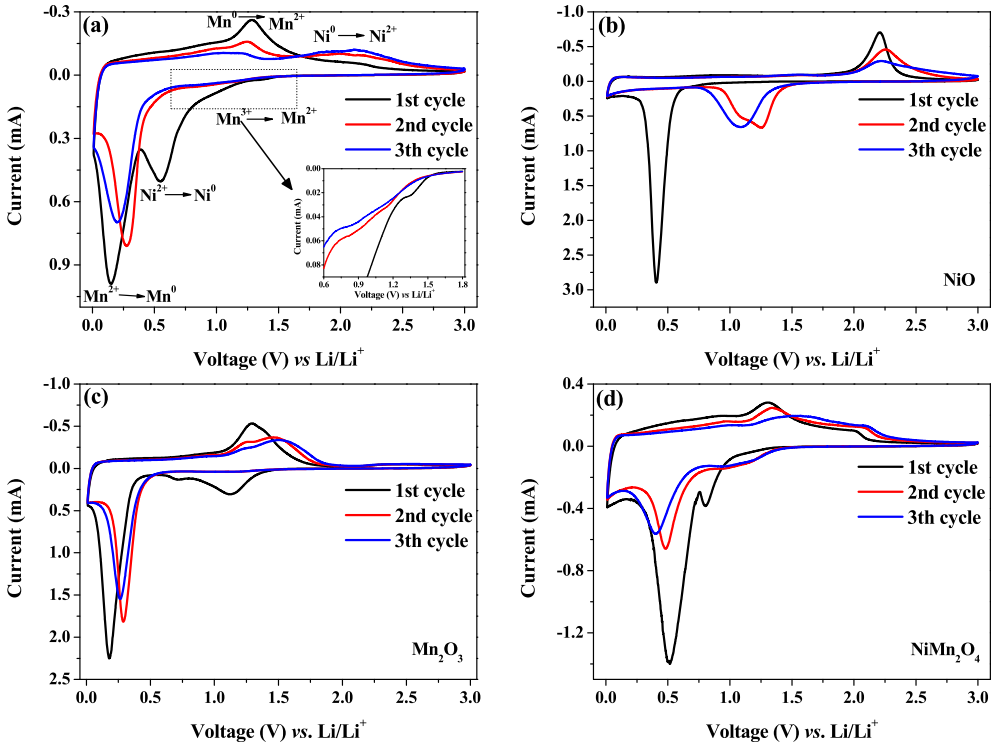

Fig. 5. Cyclic voltammograms of the anode with porous $Ni_{0.14}Mn_{0.86}O_{1.43}$ hollow microspheres (a), NiO (b), Mn_2O_3 (c) and $NiMn_2O_4$ (d) in the voltage range of 0.01–3.0 V *vs.* Li/Li^+ at a scanning rate of 0.1 mV s^{-1}.

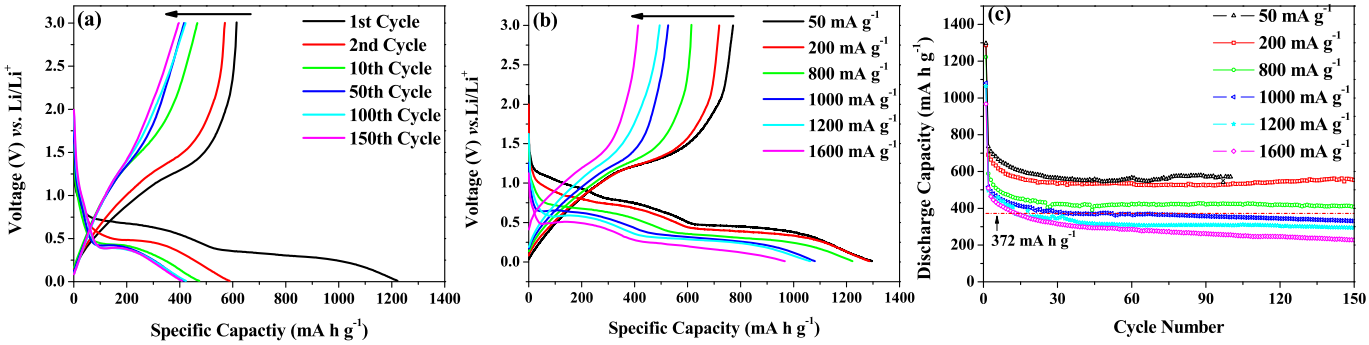

Fig. 6. Discharge/charge profiles of the anode with porous $Ni_{0.14}Mn_{0.86}O_{1.43}$ hollow microspheres at a current density of 800 mA g^{-1} (a) and at various current densities (b), cycling performance of the anode with $Ni_{0.14}Mn_{0.86}O_{1.43}$ at various current densities (c) in the voltage range of 0.01–3.0 V *vs.* Li/Li^+.

initial discharge capacity and the reversible charge capacity are as high as 1287 and 719 mA h g^{-1}, respectively. From the second cycle onwards, the discharge capacity decreases slightly and then keeps stable after about 20 cycles. A high discharge capacity of 553 mA h g^{-1} is still retained after 150 cycles. When the current density is increased to 800 mA g^{-1}, a high discharge capacity of 408 mA h g^{-1}, corresponding to 66.4% of the second discharge capacity, could be maintained after 150 cycles. This performance is significantly better than that of the anode with $Ni_{0.14}Mn_{0.86}O_{1.5}$ solid microspheres and $NiMn_2O_4$ powders, which delivers the discharge capacities of 239.6 and 284.7 mA h g^{-1}, respectively, at 800 mA g^{-1} after 100 cycles (Fig. S20 and Fig. S21). At current densities as high as 1000, 1200 and 1600 mA g^{-1}, the discharge capacities still retain at 331, 294 and 227 mA h g^{-1}, respectively, with coulombic efficiency up to about 100% after 150 cycles. The performance of the porous and hollow-structured $Ni_{0.14}Mn_{0.86}O_{1.43}$ microspheres is definitely superior to that of the conventional graphite which is widely used in commercial LIBs as anode material. Its discharge capacities of 553 and 408 mA h g^{-1} after 150 cycles at 200 and 800 mA g^{-1}, respectively, are apparently higher than the theoretical capacity of 372 mA h g^{-1} for graphite, its capacities of 331 and 294 mA h g^{-1} after 150 cycles at 1000 and 1200 mA g^{-1}, respectively, are comparable to (or even better than) the performance of graphite at ~175 mA g^{-1} (0.5 C) [45], ~115 mA g^{-1} (1/3C) [46], ~35 mA g^{-1} (0.1 C) [47,48] and ~23 mA g^{-1} (1/15 C) [49]. These results suggest that the porous and hollow-structured $Ni_{0.14}Mn_{0.86}O_{1.43}$ microspheres are promising alternatives for graphite as high-rate and long life anode for LIBs.

To date, the electrochemical properties of $NiMn_2O_4$ nanoparticles are rarely demonstrated as anode materials of LIBs, while Mn_2O_3 with micrometer-sized structure have been extensively reported [27]. For example, the $NiMn_2O_4$ nanoparticles developed by Courtel et al. [38] only delivered a capacity of 200 mA h g^{-1} after 20 cycles at 0.1 C, and that by Lavela et al. [39] demonstrated a capacity

of about 500 mA h g^{-1} after 50 cycles at 1C. However, the high-rate discharge-ability and cycling stability for longer time have not been explored and reported for $NiMn_2O_4$ nanoparticles. Qiu et al. [50] revealed that the oval-shaped and straw-sheaf-shaped Mn_2O_3 could retain capacities of 380 and 320 mA h g^{-1}, respectively, after 150 cycles, while the commercial nanoparticulate Mn_2O_3 could deliver 200 mA h g^{-1} after 50 cycles at a current density of 200 mA g^{-1}. Dai et al. [51] found that hollow Mn_2O_3 nanocones could display an initial discharge capacity of about 400 mA h g^{-1} at a current density of 400 mA g^{-1}. However, to the best of our knowledge, the uniformly dispersed nanocomposite of Mn_2O_3/$NiMn_2O_4$ has not been fabricated and reported as anode material of LIBs. Herein, we believe our work is the first effort on utilizing Mn_2O_3/$NiMn_2O_4$ nanocomposite (of 0.29 Mn_2O_3/0.14 $NiMn_2O_4$, $Ni_{0.14}Mn_{0.86}O_{1.43}$) with a hollow and porous structure as the anode material of LIBs. The excellent rate capability and stable cycling performance of the as-prepared porous and hollow-structured $Ni_{0.14}Mn_{0.86}O_{1.43}$ microspheres maybe attributed to three reasons: (1) The nanometer-sized subunits could not only enhance the electrochemical kinetics of the conversion reactions, but also improve the structure stability during the repeated charge/discharge processes [26]; (2) The porous structure is in favor of large electrode/electrolyte contact surface, short path length for electronic transport and convenient diffusion paths for ionic transport [26,52]; and (3) The hollow interior helps to relax the stress caused by the possible volume change during the repeated charge/discharge processes [53].

4. Conclusion

In summary, a facile method has been developed to produce the uniformly dispersed bi-component nanocomposite of transition metal oxide/mixed transition metal oxide (TMO/MTMO) as porous and hollow-structured microspheres based on the complexation between Ni^{2+} and NH_3. With this method, a novel TMO/MTMO composite of $Ni_{0.14}Mn_{0.86}O_{1.43}$ (0.29 Mn_2O_3/0.14 $NiMn_2O_4$) microspheres with porous and hollow structure constituted by nanometer-sized subunits was successfully prepared. The obtained $Ni_{0.14}Mn_{0.86}O_{1.43}$ microspheres exhibit reversible capacities as high as 719 and 615 mA h g^{-1} at the current densities of 200 and 800 mA g^{-1}, respectively. After 150 cycles, 408 mA h g^{-1} is still retained at 800 mA g^{-1}. The excellent electrochemical performance implies that the porous and hollow-structured $Ni_{0.14}Mn_{0.86}O_{1.43}$ microspheres are a kind of promising high-rate and long life anode for LIBs.

Acknowledgments

The authors are grateful for the financial support of this work by the National Natural Science Foundation of China (21176155 & 21476138) and Science and Technology Commission of Shanghai Municipality (14DZ2250800).

Appendix A. Supplementary data

Supplementary data related to this article can be found at http://dx.doi.org/10.1016/j.jpowsour.2015.05.021.

References

[1] K. Kang, Y.S. Meng, J. Bréger, C.P. Grey, G. Ceder, Science 311 (2006) 977–980.
[2] J.M. Tarascon, M. Armand, Nature 414 (2001) 359–367.
[3] B. Scrosati, J. Hassoun, Y.-K. Sun, Energy Environ. Sci. 4 (2011) 3287–3295.
[4] J.B. Goodenough, K.-S. Park, J. Am. Chem. Soc. 135 (2013) 1167–1176.
[5] S. Xu, C.M. Hessel, H. Ren, R. Yu, Q. Jin, M. Yang, H. Zhao, D. Wang, Energy Environ. Sci. 7 (2014) 632–637.
[6] L. Ji, Z. Lin, M. Alcoutlabi, X. Zhang, Energy Environ. Sci. 4 (2011) 2682–2699.
[7] N. Lin, Y. Han, L. Wang, J. Zhou, J. Zhou, Y. Zhu, Y. Qian, Angew. Chem. Int. Ed. 54 (2015) 3822–3825.
[8] L. Wang, L. Zhuo, C. Zhang, F. Zhao, J. Power Sources 275 (2015) 650–659.
[9] S. Ren, X. Zhao, R. Chen, M. Fichtner, J. Power Sources 260 (2014) 205–210.
[10] J. Yao, Y. Gong, S. Yang, P. Xiao, Y. Zhang, K. Keyshar, G. Ye, S. Ozden, R. Vajtai, P.M. Ajayan, ACS Appl. Mater. Inter. 6 (2014) 20414–20422.
[11] D. Cai, T. Yang, D. Wang, X. Duan, B. Liu, L. Wang, Y. Liu, Q. Li, T. Wang, Electrochim. Acta 159 (2015) 46–51.
[12] A.K. Rai, J. Gim, T.V. Thi, D. Ahn, S.J. Cho, J. Kim, J. Phys. Chem. C 118 (2014) 11234–11243.
[13] M. Shahid, N. Yesibolati, M.C. Reuter, F.M. Ross, H.N. Alshareef, J. Power Sources 263 (2014) 239–245.
[14] M. Endo, C. Kim, K. Nishimura, T. Fujino, K. Miyashita, Carbon 38 (2000) 183–197.
[15] W.-M. Zhang, J.-S. Hu, Y.-G. Guo, S.-F. Zheng, L.-S. Zhong, W.-G. Song, L.-J. Wan, Adv. Mater. 20 (2008) 1160–1165.
[16] N. Nitta, G. Yushin, Part. Part. Syst. Char. 31 (2014) 317–336.
[17] Z. Wang, L. Zhou, X.W. Lou, Adv. Mater. 24 (2012) 1903–1911.
[18] M. Armand, J.M. Tarascon, Nature 451 (2008) 652–657.
[19] A.S. Arico, P. Bruce, B. Scrosati, J.-M. Tarascon, W. van Schalkwijk, Nat. Mater. 4 (2005) 366–377.
[20] P.G. Bruce, B. Scrosati, J.-M. Tarascon, Angew. Chem. Int. Ed. 47 (2008) 2930–2946.
[21] Y.-Y. Hu, Z. Liu, K.-W. Nam, O.J. Borkiewicz, J. Cheng, X. Hua, M.T. Dunstan, X. Yu, K.M. Wiaderek, L.-S. Du, K.W. Chapman, P.J. Chupas, X.-Q. Yang, C.P. Grey, Nat. Mater. 12 (2013) 1130–1136.
[22] P. Poizot, S. Laruelle, S. Grugeon, L. Dupont, J.M. Tarascon, Nature 407 (2000) 496–499.
[23] E.W. Collings, Applied Superconductivity, Metallurgy, and Physics of Titanium Alloys, Plenum Press, New York, 1986.
[24] J.E. Huheey, E.A. Keiter, R.L. Keiter, Principles of Structure and Reactivity, fourth ed., Harper Collins College Publishers, New York, 1993.
[25] P.A. Cox, Inorganic Chemistry, second ed., Bios Scientific, London, 2004.
[26] C. Yuan, H.B. Wu, Y. Xie, X.W. Lou, Angew. Chem. Int. Ed. 53 (2014) 1488–1504.
[27] M.V. Reddy, G.V. Subba Rao, B.V.R. Chowdari, Chem. Rev. 113 (2013) 5364–5457.
[28] R. Yi, J. Feng, D. Lv, M.L. Gordin, S. Chen, D. Choi, D. Wang, Nano Energy 2 (2013) 498–504.
[29] Q.Q. Xiong, X.H. Xia, J.P. Tu, J. Chen, Y.Q. Zhang, D. Zhou, C.D. Gu, X.L. Wang, J. Power Sources 240 (2013) 344–350.
[30] R. Alcántara, M. Jaraba, P. Lavela, J.L. Tirado, Chem. Mater. 14 (2002) 2847–2848.
[31] J. Cabana, L. Monconduit, D. Larcher, M.R. Palacín, Adv. Mater. 22 (2010) E170–E192.
[32] L. Yu, L. Zhang, H.B. Wu, G. Zhang, X.W. Lou, Energy Environ. Sci. 6 (2013) 2664–2671.
[33] W. Wei, Z. Wang, Z. Liu, Y. Liu, L. He, D. Chen, A. Umar, L. Guo, J. Li, J. Power Sources 238 (2013) 376–387.
[34] L. Zhou, D. Zhao, X.W. Lou, Adv. Mater. 24 (2012) 745–748.
[35] B. Liu, J. Zhang, X. Wang, G. Chen, D. Chen, C. Zhou, G. Shen, Nano Lett. 12 (2012) 3005–3011.
[36] M. Li, Y.-X. Yin, C. Li, F. Zhang, L.-J. Wan, S. Xu, D.G. Evans, Chem. Commun. 48 (2012) 410–412.
[37] G. Huang, F. Zhang, L. Zhang, X. Du, J. Wang, L. Wang, J. Mater. Chem. A 2 (2014) 8048–8053.
[38] F.M. Courtel, H. Duncan, Y. Abu-Lebdeh, I.J. Davidson, J. Mater. Chem. 21 (2011) 10206–10218.
[39] P. Lavela, N.A. Kyeremateng, J.L. Tirado, Mater. Chem. Phys. 124 (2010) 102–108.
[40] X.-Y. Guan, J.-C. Deng, Mater. Lett. 61 (2007) 621–625.
[41] G.J. Kearley, H. Blank, Can. J. Chem. 66 (1988) 692–697.
[42] J. Guan, F. Mou, Z. Sun, W. Shi, Chem. Commun. 46 (2010) 6605–6607.
[43] H. Deng, I. Belharouak, Y.-K. Sun, K. Amine, J. Mater. Chem. 19 (2009) 4510–4516.
[44] X. Gu, L. Chen, Z. Ju, H. Xu, J. Yang, Y. Qian, Adv. Funct. Mater. 23 (2013) 4049–4056.
[45] N.S. Hochgatterer, M.R. Schweiger, S. Koller, P.R. Raimann, T. Wöhrle, C. Wurm, M. Winterc, Electrochem. Solid-State Lett. 11 (5) (2008) A76–A80.
[46] M. Gaberscek, M. Bele, J. Drofenik, R. Dominko, S. Pejovnika, Electrochem. Solid-State Lett. 3 (4) (2000) 171–173.
[47] Y. Zhang, X.G. Zhang, H.L. Zhang, Z.G. Zhao, F. Li, C. Liu, H.M. Cheng, Electrochim. Acta 51 (2006) 4994–5000.
[48] A. Trifonova, M. Winter, J.O. Besenhard, J. Power Sources 174 (2007) 800–804.
[49] B. Veeraraghavana, J. Paulb, B. Harana, B. Popov, J. Power Sources 109 (2002) 377–387.
[50] Y. Qiu, G.-L. Xu, K. Yan, H. Sun, J. Xiao, S. Yang, S.-G. Sun, L. Jin, H. Deng, J. Mater. Chem. 21 (2011) 6346–6353.
[51] Y. Dai, H. Jiang, Y. Hu, C. Li, RSC Adv. 3 (2013) 19778–19781.
[52] A. Manthiram, A. Vadivel Murugan, A. Sarkar, T. Muraliganth, Energy Environ. Sci. 1 (2008) 621–638.
[53] X.W. Lou, L.A. Archer, Z. Yang, Adv. Mater. 20 (2008) 3987–4019.